14th European Signal Processing Conference (EUSIPCO 2006), Florence, Italy, September 4-8, 2006, copyright by EURASIP

DIRECTIVITY ANALYSIS OF TIME-REVERSAL ARRAYS IN A SIMPLE OCEAN WAVEGUIDE

João Gomes *Victor Barroso*

Instituto Superior Técnico – Instituto de Sistemas e Robótica
Av. Rovisco Pais, 1049-001 Lisboa, Portugal
{jpg,vab}@isr.ist.utl.pt

ABSTRACT

This paper analyses the directivity of time-reversal arrays of arbitrary shape in a range-independent homogeneous ocean waveguide. Through feedback, these devices have the ability to focus waves in unknown media, which makes them potentially useful in many applications. The analysis is based on the image method, which expands the array into a series of reflected virtual replicas that interfere to create a strong focal spot. This setup allows the acoustic field to be approximately expressed as the product of two terms, one of which depends on the free-space directivity of the array, and the other one on the environmental properties. The former dictates the gross distribution of acoustic energy in the water column, while the latter defines the fine-scale variations and the effective size of the focus.

1. INTRODUCTION

Time reversal, or broadband phase conjugation, is a feedback wave focusing technique in which the time evolution of a propagating field is reversed, achieving spatial and temporal concentration of energy at the original source position without the need for detailed environmental knowledge. Mathematically, this property stems from the reciprocity of wave propagation in linear media, i.e., if the time variable is inverted in a solution to the wave equation, the resulting function still satisfies the wave equation. Phase conjugation originated in optics, but over time the same physical principle was applied in several other fields, such as ultrasonic materials testing, medical imaging and weakly-invasive medical therapies. Time reversal aroused keen interest as a potentially valuable tool in applications that involve active propagation in the ocean, e.g., in underwater communications [1, 2], after experiments proved the practical feasibility of this technique at medium frequencies.

Practical time reversal in the ocean relies on an array formed by several source-receiver transducers that sample the incoming pressure field generated by an acoustic source [3]. When the received signals are played back in reverse, they interfere to create a reciprocal field that converges on the original source position. All multipath replicas are thus synchronously combined at the focus, resulting in waveforms with low delay dispersion. In analogy with the reflection of light in a mirror, this type of array is known as a time-reversal mirror (TRM).

When immersed in an ocean waveguide the directive behavior of an array deviates from that of its free-space counterpart due to sound reflection at the boundaries. Understanding how array and environmental parameters interact and influence the acoustic field is important when designing practical time-reversal mirrors. While previous work in this area focused on the performance of uniform linear arrays [4, 5], it is known that nonuniformly-spaced arrays in free space can achieve the same resolution of uniform arrays of comparable size, but with a drastic reduction in the number of sensors. Albeit with more modest savings, time-reversal mirrors also benefit from nonuniform sensor spacing [6].

The present paper develops an analysis framework that accomodates both uniform and nonuniform arrays, and provides enhanced physical intuition into the propagation problem. It is shown that the acoustic field near the focal spot can be approximated by the product of two terms, one of which reflects the free-space directivity of the array, and the other depends only on the geometry of the environment, which is assumed to be range-independent and homogeneous. The free-space directivity dictates the large-scale envelope of the acoustic field, i.e., the extent of the area that is strongly insonified. The environmental term takes into account the effective augmentation in array length resulting from surface and bottom reflections. This property implies that effective synthesis tools for free-space arrays should also lead to suitable time-reversal array designs.

2. FOCUSING IN A DISCRETE MIRROR

2.1 Image Method

For the sake of analytical tractability, the ocean is modeled as a homogeneous layer bounded by the free surface $z = 0$ above and by the bottom $z = H$ below. The Helmholtz wave equation in the medium is satisfied by the free-space Green's function

$$G_{0\omega}(\mathbf{r}-\mathbf{r}') = \frac{e^{jk|\mathbf{r}-\mathbf{r}'|}}{4\pi|\mathbf{r}-\mathbf{r}'|}\,, \tag{1}$$

where $k = \omega/c$ is the wavenumber that relates the wave frequency ω and propagation speed $c \approx 1500\,\mathrm{ms}^{-1}$, $\mathbf{r}'$ denotes the source position, and $\mathbf{r}$ is the field point of interest. Because (1) does not in general satisfy the boundary conditions at the interfaces $z = 0$, $z = H$, free-space corrective terms are added by the *image method*. These may be interpreted as virtual images of the original source (multiply) reflected on the surface and bottom. The total field is written as an infinite series [7]

$$G_\omega(\mathbf{r},\mathbf{r}') = \sum_{l=-\infty}^{\infty} (-\alpha_B)^{|l|}\Big[\, G_{0\omega}(\mathbf{r}-\mathbf{r}'_{l0}) - G_{0\omega}(\mathbf{r}-\mathbf{r}'_{l1})\Big]\,, \tag{2}$$

where the surface reflection coefficient has a value of -1, the bottom reflection coefficient is denoted by α_B, and

$$\mathbf{r}'_{l0} = (r', z' + 2Hl)\,, \qquad \mathbf{r}'_{l1} = (r', -z' - 2Hl)\,.$$

2.2 Phase-Conjugate Field

The image method is used to determine the field that is received and generated by the mirror transducers located at $\mathbf{r}_m$, $m = 1, \ldots M$. The ocean cross-section is expanded into

This work was supported by the FCT Programa Operacional Sociedade da Informação (POSI) in the frame of Quadro Comunitário de Apoio III.

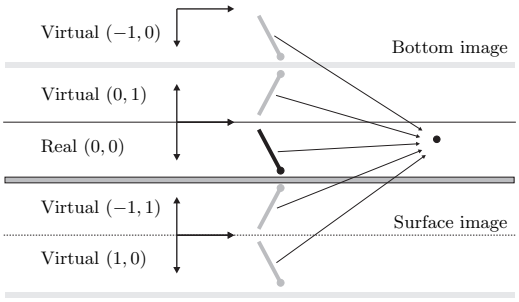

Figure 1: Array expansion into real/virtual images

multiple vertically-stacked virtual layers, and a local coordinate system is attached to each one such that the position of the m-th (virtual) sensor is always given by $\mathbf{r}_m$. As depicted in Fig. 1, the z axis direction should thus be reversed between adjacent layers. Discarding contributions from rays that undergo more than N_B bottom reflections, the series (2) may be written using local coordinates as

$$G_\omega(\mathbf{r},\mathbf{r}') = \boldsymbol{\alpha}^T\left[\mathbf{G}^{(0)}_{0\omega}(\mathbf{r},\mathbf{r}') - \mathbf{G}^{(1)}_{0\omega}(\mathbf{r},\mathbf{r}')\right] ,$$
$$\boldsymbol{\alpha} = \left[(-\alpha_B)^{|-N_B|}\ldots(-\alpha_B)^{|N_B|}\right]^T ,$$
$$\mathbf{G}^{(p)}_{0\omega}(\mathbf{r},\mathbf{r}') = \left[\begin{array}{c} G_{0\omega}(\mathbf{r}_{-N_B p}-\mathbf{r}') \\ \cdots \\ G_{0\omega}(\mathbf{r}_{N_B p}-\mathbf{r}') \end{array}\right] , \; p\in\{0,1\} ,$$
$$\mathbf{r}_{l0} = (r, z-2Hl) , \qquad \mathbf{r}_{l1} = (r, -z-2Hl) .$$

The phase-conjugated field accounts for the medium response from a source at $\mathbf{r}_s$ to the mirror transducers, and from each of those to the field point of interest $\mathbf{r}$, yielding

$$G_{c\omega}(\mathbf{r},\mathbf{r}_s) = \sum_{m=1}^{M} G^*_\omega(\mathbf{r}_m,\mathbf{r}_s)G_\omega(\mathbf{r},\mathbf{r}_m) = \boldsymbol{\alpha}^T\Big[\mathbf{B}^{(0,0)}_\omega(\mathbf{r},\mathbf{r}_s) + \mathbf{B}^{(1,1)}_\omega(\mathbf{r},\mathbf{r}_s) - 2\mathrm{Re}\Big\{\mathbf{B}^{(0,1)}_\omega(\mathbf{r},\mathbf{r}_s)\Big\}\Big]\boldsymbol{\alpha} . \quad (3)$$

By reciprocity, the spatial arguments in $\mathbf{G}^{(p)}_{0\omega}(\mathbf{r},\mathbf{r}')$ may be interchanged, resulting in the following expression for the *beamforming matrices* $\mathbf{B}_\omega$ in (3)

$$\mathbf{B}^{(p,q)}_\omega(\mathbf{r},\mathbf{r}') = \sum_{m=1}^{M} \mathbf{G}^{(p)}_{0\omega}(\mathbf{r},\mathbf{r}_m)\mathbf{G}^{(q)\,H}_{0\omega}(\mathbf{r}',\mathbf{r}_m) , \quad (4)$$

where the superscript $(\cdot)^H$ denotes conjugate transpose. As shown in [6], a plane wave approximation to the free-space Green's function can be used to write each element $-N_B \le m,n \le N_B$ of the beamforming matrix (4) as the product of a spreading term, C_ω, and an array directivity function, D_ω,

$$\left[\mathbf{B}^{(p,q)}_\omega(\mathbf{r},\mathbf{r}')\right]_{m,n} = C_\omega(|\mathbf{r}_{mp}|,|\mathbf{r}'_{nq}|)D_\omega(\hat{\mathbf{r}}_{mp}-\hat{\mathbf{r}}'_{nq}) , \quad (5)$$

$$C_\omega(r,r') = \frac{e^{jk(r-r')}}{(4\pi)^2 rr'} , \qquad D_\omega(\mathbf{r}) = \sum_{m=1}^{M} e^{-jk\langle\mathbf{r}_m,\mathbf{r}\rangle} . \quad (6)$$

2.3 Array Directivity

When $\hat{\mathbf{r}}_{mp} = \hat{\mathbf{r}}'_{nq}$ each term in the sum (6) is equal to unity, and the contributions from all elements of D_ω add in phase in this direction. In other directions the terms are not in phase, and the field is weaker. This implies that, when viewed as a function of $\mathbf{r}_{mp}$, the array is automatically phased to steer a beam in the direction of $\mathbf{r}'_{nq}$ regardless of the sensor positions $\mathbf{r}_m$. Beamforming is automatic even if these elements have random, unknown positions.

Main Lobe Properties: If the array aperture and sensor density are large enough so that D_ω is narrow and has a single main lobe, then near the source location one may ignore the beamforming matrix elements where the endpoints of $\mathbf{r}_{mp}$ and $\mathbf{r}_{s_{nq}}$ are not on the same image layer of the ocean cross-section. This includes $\mathbf{B}^{(0,1)}_\omega$ and all off-diagonal terms in $\mathbf{B}^{(0,0)}_\omega$ and $\mathbf{B}^{(1,1)}_\omega$. With that simplification the mirror is seen to operate in purely retrodirective mode, steering beams in the directions of incoming rays during the first transmision

$$G_{c\omega}(\mathbf{r},\mathbf{r}_s) = \sum_{\substack{-N_B\le l\le N_B \\ p\in\{0,1\}}} \alpha_B^{2|l|} C_\omega(|\mathbf{r}_{lp}|,|\mathbf{r}_{s_{lp}}|)D_\omega(\hat{\mathbf{r}}_{lp}-\hat{\mathbf{r}}_{s_{lp}}) . \quad (7)$$

The large-scale envelope of the focal region is mostly determined by the beampattern D_ω, while the fine-scale structure results from interference of beams, and is strongly influenced by C_ω. The physical array is thus augmented (and amplitude shaded) by its reflected images, generating a stronger and sharper focus than in free space.

At $\mathbf{r} = \mathbf{r}_s$ all beams interfere constructively, generating large pressure values. At other ranges the field will be weaker because (i) the beampatterns are no longer in phase and (ii) the spreading term C_ω in (5) becomes complex for $|\mathbf{r}| \neq |\mathbf{r}_s|$, further degrading the constructive addition of energy that would be needed to focus the field.

To gain more insight into time-reversed focusing, the contributions in layers $(l,0)$ and $(l,1)$ will now be combined. For $z \ll 2Hl$,

$$|\mathbf{r}_{l0}| = |(r,-2Hl)+(0,z)| \approx |(r,-2Hl)| - \frac{2Hlz}{|(r,-2Hl)|} , \quad (8)$$

$$|\mathbf{r}_{l1}| = |(r,-2Hl)-(0,z)| \approx |(r,-2Hl)| + \frac{2Hlz}{|(r,-2Hl)|} , \quad (9)$$

$$|\mathbf{r}_{s\,l0}| \approx |(r_s,-2Hl)| - \frac{2Hlz_s}{|(r_s,-2Hl)|} , \quad (10)$$

$$|\mathbf{r}_{s\,l1}| \approx |(r_s,-2Hl)| + \frac{2Hlz_s}{|(r_s,-2Hl)|} . \quad (11)$$

In the vicinity of $\mathbf{r}_s$ one has $|(r,-2Hl)| \approx |(r_s,-2Hl)|$, and

$$C_\omega(|\mathbf{r}_{l0}|,|\mathbf{r}_{s\,l0}|) \approx \frac{e^{-jk\frac{2Hl(z-z_s)}{|(r_s,-2Hl)|}}}{(4\pi)^2|(r_s,-2Hl)|^2} , \quad (12)$$

$$C_\omega(|\mathbf{r}_{l1}|,|\mathbf{r}_{s\,l1}|) \approx \frac{e^{jk\frac{2Hl(z-z_s)}{|(r_s,-2Hl)|}}}{(4\pi)^2|(r_s,-2Hl)|^2} = C^*_\omega(|\mathbf{r}_{l0}|,|\mathbf{r}_{s\,l0}|) . \quad (13)$$

Note that this approximation is not valid for $l=0$, as $|\mathbf{r}_{00}| = |\mathbf{r}_{01}|$ and $|\mathbf{r}_{s\,00}| = |\mathbf{r}_{s\,01}|$, so that

$$C_\omega(|\mathbf{r}_{00}|,|\mathbf{r}_{s\,00}|) = C_\omega(|\mathbf{r}_{01}|,|\mathbf{r}_{s\,01}|) = C_\omega(|\mathbf{r}|,|\mathbf{r}_s|) . \quad (14)$$

The local coordinate systems represented in Fig. 1 for layers $(l,0)$ and $(l,1)$ are defined such that their distance to the ocean surface is the same and the z axis orientation is symmetrical. Fig. 2 shows that this implies $\hat{\mathbf{r}}_{l1} - \hat{\mathbf{r}}_{s\,l1} \approx -(\hat{\mathbf{r}}_{l0} - \hat{\mathbf{r}}_{s\,l0})$ when expressed in local coordinates, hence

$$D_\omega(\hat{\mathbf{r}}_{l1} - \hat{\mathbf{r}}_{s\,l1}) \approx D_\omega(-\hat{\mathbf{r}}_{l0} + \hat{\mathbf{r}}_{s\,l0}) = D^*_\omega(\hat{\mathbf{r}}_{l0} - \hat{\mathbf{r}}_{s\,l0}) . \quad (15)$$

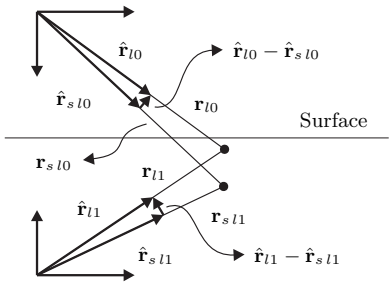

Figure 2: Coordinate systems for layers $(l, 0)$ and $(l, 1)$

Inserting (13), (14) and (15) in (7) yields

$$G_{c\omega}(\mathbf{r}, \mathbf{r}_s) \approx 2C_\omega(|\mathbf{r}|, |\mathbf{r}_s|)\mathrm{Re}\{D_\omega(\hat{\mathbf{r}} - \hat{\mathbf{r}}_s)\} + \sum_{l\neq 0} 2\alpha_B^{2|l|}\mathrm{Re}\{C_\omega(|\mathbf{r}_{l0}|, |\mathbf{r}_{s\,l0}|)D_\omega(\hat{\mathbf{r}}_{l0} - \hat{\mathbf{r}}_{s\,l0})\}\,. \quad (16)$$

Similarly to what was done for layers $(l, 0)$ and $(l, 1)$, it is now possible to combine the terms for $\pm l$ (i.e., the four layers $(\pm l, 0/1)$) in (16). Using (8) and (10) in (6) for $-l$ yields, as in (13),

$$C_\omega(|\mathbf{r}_{-l0}|, |\mathbf{r}_{s\,-l0}|) \approx \frac{e^{jk\frac{2Hl(z-z_s)}{|(r_s,2Hl)|}}}{(4\pi)^2|(r_s, 2Hl)|^2} = C^*_\omega(|\mathbf{r}_{l0}|, |\mathbf{r}_{s\,l0}|)\,. \quad (17)$$

The last line in (17) follows from $|(r_s, 2Hl)| = |(r_s, -2Hl)|$. Regarding the directivity function D_ω, observe that, when $\mathbf{r} \approx \mathbf{r_s}$,

$$\hat{r}_{-l0} - \hat{r}_{s\,-l0} \approx \frac{(r_s, 2Hl) + (0, z)}{|(r_s, 2Hl)|} - \frac{(r_s, 2Hl) + (0, z_s)}{|(r_s, 2Hl)|} = \frac{(0, z - z_s)}{|(r_s, 2Hl)|} \approx \hat{r}_{l0} - \hat{r}_{s\,l0}\,, \quad (18)$$

hence

$$D_\omega(\hat{r}_{-l0} - \hat{r}_{s\,-l0}) \approx D_\omega(\hat{r}_{l0} - \hat{r}_{s\,l0})\,. \quad (19)$$

Using (17) and (19) in (16) results in the simplified field

$$G_{c\omega}(\mathbf{r}, \mathbf{r}_s) \approx 2C_\omega(|\mathbf{r}|, |\mathbf{r}_s|)\mathrm{Re}\{D_\omega(\hat{\mathbf{r}} - \hat{\mathbf{r}}_s)\} + \sum_{l=1}^{N_B} 4\alpha_B^{2l}\mathrm{Re}\{C_\omega(|\mathbf{r}_{l0}|, |\mathbf{r}_{s\,l0}|)\}\mathrm{Re}\{D_\omega(\hat{\mathbf{r}}_{l0} - \hat{\mathbf{r}}_{s\,l0})\}\,. \quad (20)$$

As noted above, phase conjugation steers all array images such that their main lobes align at the focus in $\mathbf{r}_s$. Moreover, as $|l|$ increases the images are gradually steered away from broadside, which increases their main lobe width. As the focal spot is always much narrower than the main lobe of D_ω, in that region it is possible to write $D_\omega(\hat{\mathbf{r}}_{l0} - \hat{\mathbf{r}}_{s\,l0}) \approx D_\omega(\hat{\mathbf{r}} - \hat{\mathbf{r}}_s)$ and factor it as follows

$$G_{c\omega}(\mathbf{r}, \mathbf{r}_s) \approx 2\mathrm{Re}\{D_\omega(\hat{\mathbf{r}} - \hat{\mathbf{r}}_s)\}E_\omega(\mathbf{r}, \mathbf{r}_s)\,, \quad (21)$$

$$E_\omega(\mathbf{r}, \mathbf{r}_s) = C_\omega(|\mathbf{r}|, |\mathbf{r}_s|) + \sum_{l=1}^{N_B} 2\alpha_B^{2l}\mathrm{Re}\{C_\omega(|\mathbf{r}_{l0}|, |\mathbf{r}_{s\,l0}|)\}\,. \quad (22)$$

The following remarks can be made about (21)–(22):

- The rapid variations in E_ω due to interference among the spreading terms essentially dictate the width of the focal spot regardless of the sensor positions.
- The large-scale envelope of the acoustic field in the vicinity of the focus is determined by the free-space array beampattern D_ω, and is not influenced by the surrounding medium.
- The factorization of $G_{c\omega}$ suggests that effective strategies for designing free-space beampatterns should also be useful in the context of time-reversal.

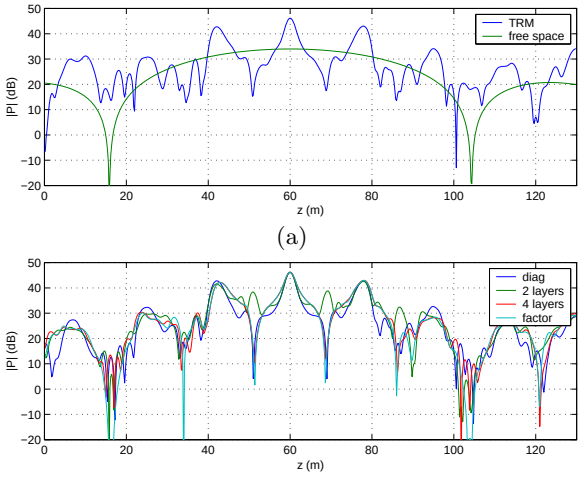

Figure 3: Uniform vertical array: 1 kHz, $M = 50$, $z_m = 40$–90 m (a) Full field (b) Approximations

Sidelobe Region: Outside the main lobe region C_ω introduces fast phase variations that randomize the entries of the beamforming matrices (4). Moreover, the diagonal approximation of $\mathbf{B}_\omega^{(0,0)}$ and $\mathbf{B}_\omega^{(1,1)}$ is no longer accurate because there is no guarantee that the directivity functions D_ω will be evaluated in the main lobe region for any of the entries. These matrices, as well as $\mathbf{B}_\omega^{(0,1)}$, are more appropriately described as having i.i.d. entries. This suggests that the sidelobe distribution is unstructured, and sidelobe properties such as amplitude and density should depend weakly on the acoustic frequency under most operating scenarios of interest. A detailed statistical study of beampattern properties in that region is beyond the scope of this paper.

3. SIMULATION RESULTS

A simulation study was conducted to validate the expressions that were obtained for the acoustic field. The chosen scenario is a range-independent ocean cross section with depth $H = 130$ m, source-mirror range $r_s = 1.5$ km, source depth $z_s = 60$m, uniform sound speed $c = 1500\mathrm{ms}^{-1}$, bottom reflectivity $\alpha_B = 0.6$ and image truncation limit $N_B = 10$.

Fig. 3a shows the conjugated acoustic field generated by a vertical mirror with $M = 50$ uniformly-distributed transducers between 40 and 90 m at $f = 1$ kHz, as well as the free-space directivity function D_ω over the equivalent angular region. To simplify the representation, conjugated pressure values were normalized by $(4\pi r_s)^2$ to approximately cancel the denominator of C_ω in (6). Fig. 3b shows the approximate fields calculated according to (7) (diag), (16) (2 layers), (20) (4 layers) and (21) (factor). The shape of the high-intensity region between 40 and 80 m is reasonably well approximated, especially the narrow peak at $z_s = 60$ m and the two others surrounding it. In light of (21) and the relative flatness of D_ω in that region, the shape of $G_{c\omega}$ is seen to be determined mostly by C_ω.

Fig. 4 shows similar results for $f = 2$ kHz. The high-intensity region is now halved, but the same general con-

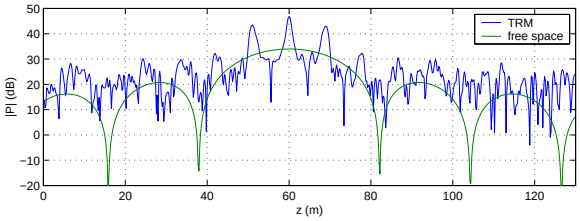

(a)

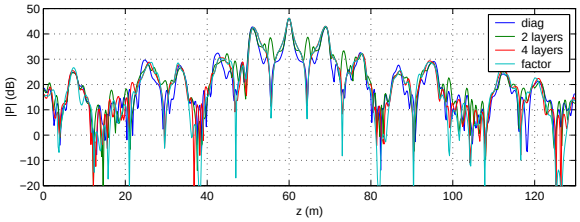

(b)

Figure 4: Uniform vertical array: 2 kHz, $M = 50$, $z_m = 40$–90 m (a) Full field (b) Approximations

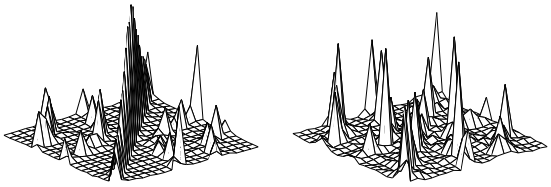

(a) (b)

Figure 5: Beamforming matrices calculated at (a) (r_s, z_s) (b) $(r_s, z = 20\,\mathrm{m})$

clusions drawn earlier remain valid. The discrepancies between the conjugated field and the approximations of Fig. 4b increase in the sidelobe region, where beamforming matrices are far from diagonal. Fig. 5 illustrates this for $\mathbf{B}^{(0,0)}+\mathbf{B}^{(1,1)}-2\mathrm{Re}\{\mathbf{B}^{(0,1)}\}$ calculated at (r_s, z_s) and $(r_s, z = 20\,\mathrm{m})$.

Being determined mainly by C_ω, the shape of the focal spot should be relatively insensitive to the directivity function D_ω. Fig. 6 confirms this for the same conditions of Fig. 4, but with $M = 50$ randomly-spaced transducers (uniform pdf) between 40 and 90 m. Note how the three main pressure peaks are preserved, even though the underlying array directivity function changes significantly.

Finally, Fig. 7 shows the pressure field generated by a sparser uniform mirror, with $M = 30$ sensors spanning the water column. In spite of the large intersensor separation ($3.3\,\lambda$), no grating lobes are present in the narrow visible range. As expected, the main peak at z_s retains the same shape of Figs. 4 and 6. In accordance with the factorization

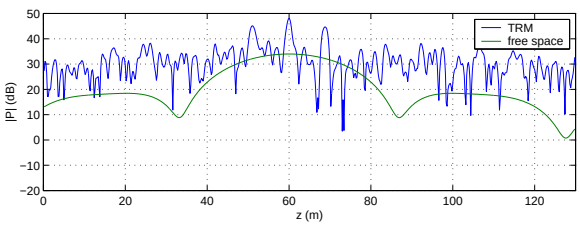

Figure 6: Random vertical array: 2 kHz, $M = 50$, $z_m = 40$–90 m

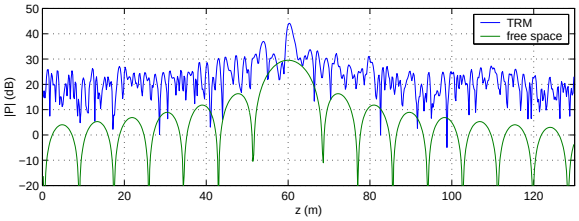

(a)

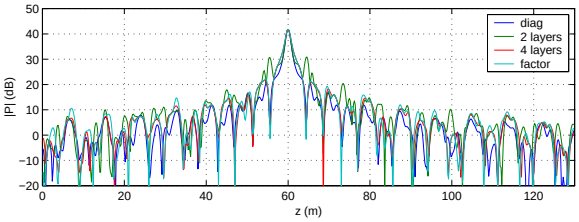

(b)

Figure 7: Uniform vertical array: 2 kHz, $M = 30$, $z_m = 1$–129 m (a) Full field (b) Approximations

result (21), the two secondary peaks that were previously present in $G_{c\omega}$ are now suppressed by the narrower directivity function.

4. CONCLUSION

The image method was used as a tool to analyze the directivity of arbitrarily-shaped time-reversal arrays. Theoretical results indicate that a decoupling property holds near the focal spot, allowing the field to be approximately expressed as the product of a term that reflects the array properties by another one which depends only on the environment. Simulation results validated these predictions for uniform and randomly-spaced vertical arrays. Future work will attempt to characterize the statistical behavior of the acoustic field in the sidelobe region.

REFERENCES

[1] J. Flynn *et al.*, "Multichannel equalization by decision-directed passive phase conjugation: Experimental results," *IEEE J. Oceanic Eng.*, vol. 29, no. 3, pp. 824–836, Jul. 2004.

[2] G. Edelmann *et al.*, "An initial demonstration of underwater acoustic communication using time reversal," *IEEE J. Oceanic Eng.*, vol. 27, no. 3, pp. 602–609, Jul. 2002.

[3] D. Jackson, D. Dowling, "Phase conjugation in underwater acoustics," *J. Acoust. Soc. Am.*, vol. 89, no. 1, pp. 171–181, Jan. 1991.

[4] J. Gomes, V. Barroso, "Using phase conjugation for underwater acoustic communication: Design guidelines," in *Proc. of the X European Signal Processing Conference (EUSIPCO'00)*, Tampere, Finland, Sept. 2000.

[5] J. Gomes, V. Barroso, "Ray-based analysis of a time-reversal mirror for underwater acoustic communication," in *Proc. ICASSP'00*, Istanbul, Turkey, June 2000.

[6] J. Gomes, V. Barroso, "The performance of sparse time-reversal mirrors in the context of underwater communications," in *Proc. 10th IEEE Workshop on SSAP*, Pocono, PA, Aug. 2000.

[7] L. Brekhovskikh, Y. Lysanov, *Fundamentals of Ocean Acoustics*, Springer-Verlag, second ed., 1991.